

Article

# Research on Detent Force Characteristics of Winding Segmented Permanent Magnet Linear Synchronous Motor Based on Analytical Model

Tuanshan Zhang <sup>1,2</sup>  and Xuesong Mei <sup>1,\*</sup> 

<sup>1</sup> Department of Mechanical Engineering, Xi'an Jiaotong University, Xi'an 710049, China; zhangtuanshan@xpu.edu.cn

<sup>2</sup> Department of Mechanical and Electrical Engineering, Xi'an Polytechnic University, Xi'an 710048, China

\* Correspondence: xsmei@mail.xjtu.edu.cn

**Abstract:** The winding segmented permanent magnet linear synchronous motor (WS-PMLSM) has not only a general slotting effect but also a unique two-end effect caused by the segmented stator and the finite length passive mover, which makes the detent force of WS-PMLSM possess the qualities of all types of linear motors. This paper adopts a physics-based multiple analytical method to study the detent force properties. First, an accurate sub-domain model is used to obtain the magnetic field distribution of the tooth slot, and the results of the analytical solution and the graph of the tooth slot effect are obtained using the scalar magnetic potential. Subsequently, the effect of the end unenergized core on the magnetic field is analyzed using Maxwell's theory for the stator end effect, revealing that the end effect causes pulsating and reversing magnetic fields in the motor, which in turn creates mutual inductance with unequal phases, and generates thrust fluctuations. Finally, a complex relative air-gap permeability is introduced on the basis of the conformal mapping to equate the end effect generated by the permanent magnet. The accuracy of the proposed multiple analytical models was verified by the results of the finite element method (FEM) and experimental model.

**Keywords:** winding segmented permanent magnet linear synchronous motor (WS-PMLSM); detent force; two-end effect; slotting effect; accurate sub-domain model; conformal mapping



**Citation:** Zhang, T.; Mei, X. Research on Detent Force Characteristics of Winding Segmented Permanent Magnet Linear Synchronous Motor Based on Analytical Model. *Symmetry* **2022**, *14*, 1049. <https://doi.org/10.3390/sym14051049>

Academic Editor: Alexander Zaslavski

Received: 21 April 2022

Accepted: 15 May 2022

Published: 20 May 2022

**Publisher's Note:** MDPI stays neutral with regard to jurisdictional claims in published maps and institutional affiliations.



**Copyright:** © 2022 by the authors. Licensee MDPI, Basel, Switzerland. This article is an open access article distributed under the terms and conditions of the Creative Commons Attribution (CC BY) license (<https://creativecommons.org/licenses/by/4.0/>).

## 1. Introduction

An important application of winding segmented permanent magnet linear synchronous motors (WS-PMLSM) in modern industry is material handling and processing [1]. The main purpose is to reduce labor. A common form is made into a ring structure so that it can be recycled, and the transmission moving parts are called movers, which are passive and do not require any energy or information transfer. The track consists of segmented stators, equivalent to multiple motors connected in series, each stator being separately powered and controlled [2]. Figure 1 shows an example of an application in a battery-powered line, where multiple movers operate highly independently on the same track, with four stations (P1–P4) distributed along the track at the desired locations [3].

Obviously, the detent force of WS-PMLSM is a problem in the processing area, and it also tends to cause workpiece loosening and running noise, which seriously affects the smoothness of the transfer system and is even more impermissible in the case of transferring liquids. This detent force is mainly caused by the slot effect and the longitudinal end effect [4]. The slot effect is more common and the corresponding literature is more abundant. This literature can be summarized into two methods; one is to improve the motor structure [5–8], and the other is to use special control methods [9–11].

However, compared to conventional linear motors, the WS-PMLSM generates two types of end effects, defined as secondary end effects and primary end effects, due to the limited length of the secondary module of the permanent magnet and the primary

module of the winding, which increases the complexity of implementing thrust fluctuation suppression for such motors.

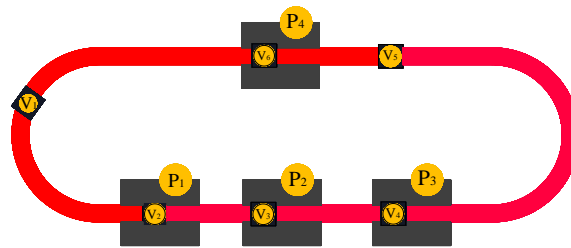


**Figure 1.** WS-PMLSM for transmission lines.

The secondary end effect is an important factor for the thrust fluctuation generated by WS-PMLSM, which is also a unique phenomenon of WS-PMLSM [12]. It is caused by the magnetic field of the permanent magnets at the secondary end, mainly in the form of the magnetic field of the secondary pole affecting the magnetic field distribution inside the motor through the magnetic field association of the adjacent poles.

The primary end effect is related to the discontinuous distribution of the winding, similar to the commonly analyzed end effect in linear induction motors [13], but it is reflected in the change of electromagnetic parameters only when there is a current excitation in the winding, due to the abnormal magnetic field distribution at the end [14]. Due to the presence of closely connected cores outside the energized modules and the variation of magnetic fields, less of the literature has focused on this aspect.

To effectively predict the detent forces due to end effects and slotting effects, different methods have been developed, which can be divided into four main categories: analytical, semi-analytical, numerical, and hybrid methods (a combination of all three) [15]. Numerical methods are very flexible for a wide range of geometries, including nonlinear and non-homogeneous materials, and can be combined with other physics. One of the more representative numerical methods is the FEM [16,17]; however, the high level of complexity in FEM leads to very time-consuming simulations that slow down the design process. Therefore, it seems necessary to develop a simple analytical model for the initial design that is very fast in computation and provides more physical insight. Several analytical methods have been proposed, such as the magnetic circuit method [18], the hierarchical model method [19], the integral transformation method [20], the field-circuit coupled method [21], the air gap magnetic permeability method, the winding function method [22] and the Maxwell mathematical physics method [23]. Among all analytical techniques, a semi-analytical method called the subdomain model (SDM) has been developed that can calculate magnetic fields very accurately and much faster than numerical methods (e.g., FEM), making it a good method to study and deploy.

The SDM approach is to simplify the motor model by dividing it into several regular domains in which the problem is linearized. Liu et al. [24] first introduced an accurate subdomain modeling approach for slot models with pole pair conversion. Guo and Hu [25] proposed a new analytical model for long dynamic magnetic linear motors, which uses a method that scales up the diameter of the rotating motor to a certain degree so as to approach the linear motor model, the results obtained from this analytical model depend on the choice of radius. An effective analytical model for PMLSM is presented in [26,27], which takes into account the end effects by adding virtual slots and slotting effects by using relative air-gap permeability. These methods try to solve all magnetic resistance problems of linear motors; however, the nonlinear magnetic field distribution at the end of WS-PMLSM requires the division of more subdomains. Therefore, in this paper, only the slotting effect is studied by using the mature SDM method, and the end effect is analyzed by other methods.

In view of the limitations of SDM in the application of WS-PMLSM, it is necessary to integrate various magnetic field solution methods to analyze and study the end effect of

WS-PMLSM magnetically. The Conformal Map Method (CM) [28] is a powerful analytical tool for determining two-dimensional magnetic fields. Using the CM method, a complex magnetic field structure can be transformed into a simpler linear magnetic field structure so that it is easier to solve the differential equations. For example, a special CM, called the Schwarz–Christoffel (SC) mapping method [29], is used to determine end effects, but all of the literature is on linear-induced motors, and there is very little literature on linear motors where the secondary is a permanent magnet.

For the end effect of WS-PMLSM with open core and segmented power supply, there is even less literature, generally using the direct table look-up method of current-flux linkage [30,31], FEM [32], etc. The WS-PMLSM has the process of moving through the stator armature segmentation [10] and also the pulsating air gap magnetic field caused by the inductance imbalance caused by the adjacent segmented cores [33], which further complicates the end effect.

In this paper, multi-analysis models of WS-PMLSM considering the effect of both ends, and the effect of the slot are proposed. In Section 2, the effect of the slot is analyzed with an exact subdomain model, and the SD model of the SW-PMLSM is developed to derive the analytical solution of the air-gap density and obtain the detent force of the slot. In Section 3, the secondary end effect is further investigated based on the conformal map and the complex relative air-gap permeability, which leads to the derivation of the effect law of the permanent magnet end on the detent force. In Section 4, based on the classical magnetic potential theory, the magnetic potential of the single-phase winding is derived by considering the energized section of the stator and the non-energized stator at its two ends as a whole, which leads to end effects in the windings. In Section 5, the relevant conclusions are verified by finite elements and experiments.

## 2. Analysis of the Slot Effect

The effect of the slots is analyzed using an accurate subdomain model in which a scalar magnetic potential is used so that the effect of the slots can be simulated using the magnetic field distribution in each subdomain.

### 2.1. Basic Assumptions

The following basic assumptions are made for WS-PMLSM, the structure is as Figure 2.

1. The permeability of the core and support of the stator is infinite.
2. The permeability of the permanent magnet is equal to the permeability of the air, i.e.,  $\mu_r = \mu_0$ .
3. Permanent magnet conductivity and eddy currents are ignored.
4. The motor is symmetric and the effect in the  $z$ -direction is negligible.
5. Permanent magnets can only be magnetized in the  $x$ - or  $y$ -direction.

The exact subdomain model of WS-PMLSM is shown in Figure 3. Where  $l_m$  is the pole length,  $\tau$  is the pole pitch,  $h_m$  is the permanent magnet height,  $\delta$  is the air gap length,  $h_s$  is the slot height,  $b_s$  is the slot width,  $b_t$  is the tooth width,  $t_s$  is the tooth pitch, and the total number of slots is  $z_1$ .

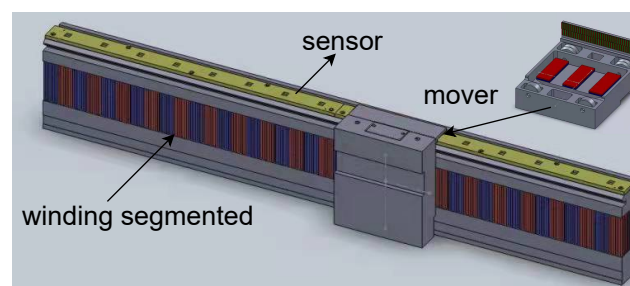


Figure 2. Structure of the WS-PMLSM.

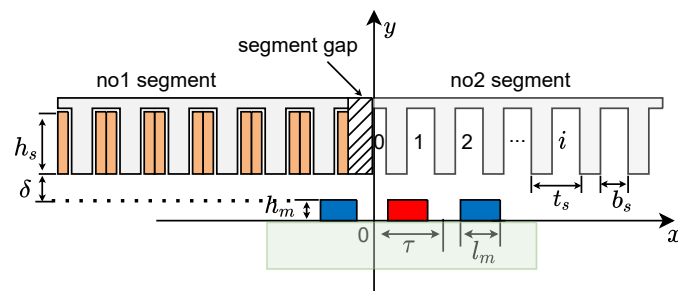


Figure 3. WS-PMLSM exact sub-domain model.

The relationship between the magnetic flux density  $B$  and the magnetic field strength  $H$  in the region of air and permanent magnets is as follows.

In the PM subdomain

$$\vec{B}_1 = \mu_0 \mu_r \vec{H}_1 + \mu_0 \vec{M} \quad (1)$$

In the air gap subdomain

$$\vec{B} = \mu_0 \vec{H} \quad (2)$$

where  $\mu_r$  is the relative permeability of PM,  $\mu_0$  is the permeability of air gap,  $\vec{M}$  is the magnetization of PM. In this way, the vector equation of PM can be written in the following form:

$$\vec{M} = M_x \vec{i} + M_y \vec{j} \quad (3)$$

where  $M_x$  and  $M_y$  denote the components of  $\vec{M}$  in the  $x$ - and  $y$ - directions, respectively, and  $i$  and  $j$  are the unit vectors in the  $x$ - and  $y$ - directions, and in this paper,  $M_x = 0$ .

Currently, there are two main methods for the numerical solution of the permanent magnetic field. One is to use the vector magnetic potential  $\vec{A}$  as the solution variable of the whole solution field, and this algorithm has many degrees of freedom, takes up a large amount of memory, takes a long time to solve, and requires high computer resources; the other is to use the scalar magnetic potential  $\phi$  as the solution variable of the solution field, and this algorithm has the advantages of fewer variables, less memory, and fast computation. Therefore, the scalar magnetic potential  $\phi$  is used to describe the magnetic field distribution, the magnetic field strength can be expressed in terms of the magnetic scalar potential as follows:

$$H_x = -\frac{\partial \phi}{\partial x} \quad H_y = -\frac{\partial \phi}{\partial y} \quad (4)$$

The number of slots under a pair of poles is:

$$z_p = \frac{z_1}{p} \quad (5)$$

where  $p$  is the number of polar pairs. Taking the center of the  $z_p$ th slot as the initial position and fixing the two-dimensional Cartesian coordinates on the stator, the initial position of the  $i$ th slot is defined as:

$$x_i = -\frac{b_s}{2} + t_s(i-1) \quad i = 1, 2, \dots, z_p \quad (6)$$

## 2.2. Scalar Magnetic Potential Flux Solution for Each Subdomain

According to the relationship between the flux density and the magnetic field strength, the magnetic field of the motor can be divided into three regions: permanent magnet subdomain-1, air gap subdomain-2 and slot subdomain-3i ( $i = 1, 2, \dots, z_p$ ).

Here, Cartesian coordinates are used to calculate the magnetic field, and when the Laplace equation is used for each of the above three subdomains with the scalar magnetic potential as the variable, the control equation for each subdomain is as follows.

### 2.2.1. The PM Subdomain

According to Equation (1), the scalar magnetic potential  $\phi$  of region 1 can be rewritten as:

$$\nabla \cdot \vec{B}_1 = \mu_0 \mu_r (-\nabla^2 \phi_1) + \nabla \cdot \mu_0 \vec{M} = 0 \quad (7)$$

$$\nabla^2 \phi_1 = \frac{\nabla \cdot \vec{H}_1}{\mu_r} \quad (8)$$

Since the magnet pole is magnetized only in the Y direction,  $M_x = 0$ , and for the convenience of description, let  $M(x) = M_y(x)$ , the magnetization intensity distribution function is shown in Figure 4.

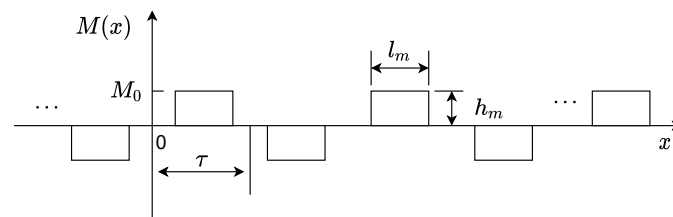


**Figure 4.** Magnetization intensity distribution function.

The permanent magnet is equated to the magnetization intensity distribution function  $M(x)$ , for which a Fourier series expansion is performed to obtain [34]:

$$M(x) = \sum_{n=1,3,\dots} M_n \sin(K_n(x - x_0)) \quad (9)$$

where

$$M_n = (-1)^{\frac{n+3}{2}} \frac{4}{n\pi} M_0 \sin\left(\frac{n\pi}{2} \alpha_p\right) \quad (10)$$

where  $\alpha_p$  is the permanent magnet pole arc coefficient,  $x_0$  is the initial position of the PM mover,  $\alpha_p = l_m/\tau$ ,  $M_0$  is the permanent magnet magnetization strength,  $M_0 = B_r/\mu_0$ ,  $B_r$  is the permanent magnet remanence,  $\mu_0$  is the air permeability, and  $k_n = n\pi/\tau$ . Let  $a = h_m$ ,  $b = h_m + \delta$ ,  $c = h_m + \delta + h_s$ , yield:  $b = a + \delta$ ,  $c = b + h_s = a + \delta + h_s$ . Therefore, the  $M(x)$  can also be expanded to the following equation:

$$M(x) = \sum_{n=1,2,3,\dots} [M_{xns} \sin(K_n x) - M_{xnc} \cos(K_n x)] \quad (11)$$

$$\begin{cases} M_{xns} = M_n \cos(K_n x_0) \\ M_{xnc} = M_n \sin(K_n x_0) \end{cases} \quad (12)$$

$$\nabla \cdot \vec{M} = \frac{\partial M_x}{\partial x} + \frac{\partial M_y}{\partial y} = 0 \quad (13)$$

According to Equation (8), the Poisson equation for the PM region can be written as:

$$\frac{\partial^2 \phi_1}{\partial x^2} + \frac{\partial^2 \phi_1}{\partial y^2} = 0 \quad (14)$$

### 2.2.2. The Air Gap and Slot Regions

The scalar magnetic potential of air gap subdomain 2:

$$\frac{\partial^2 \phi_2}{\partial x^2} + \frac{\partial^2 \phi_2}{\partial y^2} = 0 \quad (15)$$

The  $i$ th ( $i = 1, 2, \dots, z_p$ ) slot subdomain  $3i$ :

$$\frac{\partial^2 \phi_{3i}}{\partial x^2} + \frac{\partial^2 \phi_{3i}}{\partial y^2} = 0 \quad (16)$$

The permanent magnet subdomain 1 scalar magnetic potential flux solution [35] is

$$\begin{aligned} \phi_1(x, y) = & \sum_{n=1,2,\dots}^{\infty} \left[ A_1(n)e^{k_n y} + B_1(n)e^{-k_n y} \right] \cos(k_n x) + \\ & \sum_{n=1,2,\dots}^{\infty} \left[ C_1(n)e^{k_n y} + D_1(n)e^{-k_n y} \right] \sin(k_n x) \end{aligned} \quad (17)$$

The air gap subdomain 2 scalar magnetic potential flux solution is

$$\begin{aligned} \phi_2(x, y) = & \sum_{n=1,2,\dots}^{\infty} \left[ A_2(n)e^{k_n y} + B_2(n)e^{-k_n y} \right] \cos(k_n x) + \\ & \sum_{n=1,2,\dots}^{\infty} \left[ C_2(n)e^{k_n y} + D_2(n)e^{-k_n y} \right] \sin(k_n x) \end{aligned} \quad (18)$$

For the slot region, assuming that the depth of the slot is infinite, the boundary conditions for the scalar magnetic potential are as follows:

$$\phi_{3i} = \begin{cases} 0, & x = x_i \\ 0, & x = x_i + b_s \\ \phi_s(x, y), & y = b \\ 0, & y = c \end{cases} \quad (19)$$

where  $\phi_s(x, y)$  is the magnetic potential of the toothed surface.

$$\phi_{3i} = \sum_m \left[ C_{3i}(m)e^{F_m y} + D_{3i}(m)e^{-F_m y} \right] \cdot \sin[F_m(x - x_i)] \quad (20)$$

where  $F_m = (m\pi/b_s)$ . Due to  $\phi_{3i}|_{y=+\infty} = 0$ , so  $C_3 = 0$ , Equation (20) can also be written as:

$$\phi_{3i} = \sum_m D_{3i}(m)e^{-F_m y} \sin[F_m(x - x_i)] \quad (21)$$

### 2.3. Boundary Conditions

As shown in Figure 3, according to the relationship between the boundaries of each sub-domain, the equations of the coefficients of each boundary condition are established. The boundary conditions at the junction of each sub-domain are as follows:

$$\begin{cases} H_{1x}|_{y=0} = 0 \\ H_{1x}|_{y=h_m} = H_{2x}|_{y=h_m} \\ B_{1y}|_{y=h_m} = B_{2y}|_{y=h_m} \end{cases} \quad (22)$$

Furthermore, on the interface between the stator and the air gap:

$$H_{3ix}|_{y=h_m+\delta} = \begin{cases} H_{2x}|_{y=h_m+\delta} & x \in [x_i, x_i + b_s] \\ 0 \end{cases} \quad (23)$$

$$B_{3iy}|_{y=h_m+\delta} = B_{2y}|_{y=h_m+\delta} \quad (24)$$

By applying the above boundary conditions and interface conditions, the unknown coefficients from  $A_1$  to  $D_1$  and from  $A_2$  to  $D_2$  can be determined, and the derivation process can be referred to in Appendix A.

### 2.4. Analysis of Magnetic Fields in Each Subdomain

Substituting  $A_1(n), B_1(n), C_1(n), D_1(n), A_2(n), B_2(n), C_2(n), D_2(n)$  into  $\phi_1(x, y), \phi_2(x, y)$  and  $\phi_3(x, y)$  gives the magnetic potential of each subdomain. According to the relationship between scalar magnetic potential and magnetic density:

$$B_{1y}(x, y) = -\mu_0\mu_r \left\{ \sum_{n=1,2}^{\infty} k_n \left[ A_1(n)e^{k_n y} - B_1(n)e^{-k_n y} \right] \cos(k_n x) + \sum_{n=1,2}^{\infty} k_n \left[ C_1(n)e^{k_n y} - D_1(n)e^{-k_n y} \right] \sin(k_n x) \right\} + \mu_0 M_y(x) \tag{25}$$

$$B_{1x}(x, y) = -\mu_0\mu_r \left\{ \sum_{n=1,2,\dots}^{\infty} k_n \left[ A_1(n)e^{k_n y} + B_1(n)e^{-k_n y} \right] [-\sin(k_n x)] + \sum_{n=1,2,\dots}^{\infty} k_n \left[ C_1(n)e^{k_n y} + D_1(n)e^{-k_n y} \right] \cos(k_n x) \right\} \tag{26}$$

$$B_{2y}(x, y) = -\mu_0 \left\{ \sum_{n=1,2,\dots}^{\infty} k_n \left[ A_2(n)e^{k_n y} - B_2(n)e^{-k_n y} \right] \cos(k_n x) + \sum_{n=1,2,\dots}^{\infty} k_n \left[ C_2(n)e^{k_n y} - D_2(n)e^{-k_n y} \right] \sin(k_n x) \right\} \tag{27}$$

$$B_{2x}(x, y) = -\mu_0 \left\{ \sum_{n=1,2}^{\infty} k_n \left[ A_2(n)e^{k_n y} + B_2(n)e^{-k_n y} \right] [-\sin(k_n x)] + \sum_{n=1,2,\dots}^{\infty} k_n \left[ C_2(n)e^{k_n y} + D_2(n)e^{-k_n y} \right] \cos(k_n x) \right\} \tag{28}$$

$$B_{3iy}(x, y) = -\mu_0 \sum_{m=1,2}^{\infty} C_{3i}(m) F_m e^{F_m y} \left[ 1 + e^{2F_m(c-y)} \right] \sin[F_m(x - x_i)] \tag{29}$$

$$B_{3ix}(x, y) = -\mu_0 \sum_{m=1,2,\dots}^{\infty} C_{3i}(m) F_m e^{F_m y} \left[ 1 + e^{2F_m(c-y)} \right] \cos[F_m(x - x_i)] \tag{30}$$

### 3. Analysis of Windings End Effect

Figure 5 shows a WS-PMLSM model with a three-phase full-pitch winding and an effective pole number of  $2p$ . To simplify the calculation process, Where  $a, b, c$  are the magnetic flux paths of the three regions,  $\tau$  is the pole pitch,  $H_c$  is the stator height,  $\delta$  is the air gap length. the following assumptions are made:

1. Neglecting the gearing effect of the winding, the magnetic field generated by each phase winding in the air gap can be seen as a result of the traveling wave current layer generated;
2. The magnetic field at  $x < -l$  or  $x > 2l$  is zero, the studied motor section is divided into three regions: ①, ②, ③, where the energized region is ①, and the non-energized regions are ①, ②
3. The air gap contains only the  $y$ -direction magnetic field, and the gap between segments is ignored.

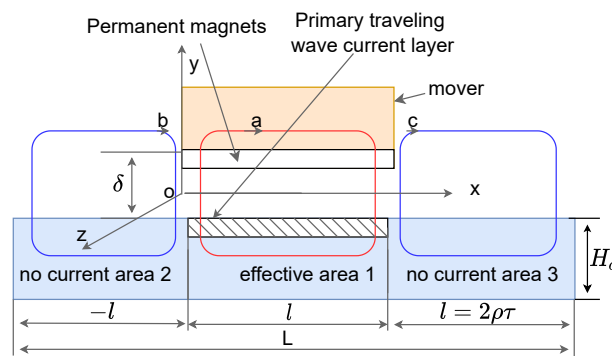


Figure 5. Primary side end effect model diagram.

*Magnetic Field Equation*

In zone ①, the equivalent piece line current density:

$$j_1 = J_{sm} \sin(\omega t - \alpha x) \tag{31}$$

When considering only region ①:

$$\begin{cases} B_{y1}(t) = B_m \cos(\omega t - \alpha x) + c \\ B_m = \frac{\mu_0 \tau}{\pi g_s} J_{sm} \end{cases} \tag{32}$$

where  $\alpha = \pi/\tau$ ,  $c$  is the end effect of ②, ③ on ①,  $J_{sm}$  is the equivalent piece line current density amplitude,  $\tau$  is the motor pole pitch,  $\omega$  is the power supply angular frequency, applying Ampere’s law of cycles along the circuit shown yields:

$$\frac{B_{y0}(t)g_s}{\mu_0} - \frac{B_{y1}(t)g_s}{\mu_0} = \int_0^x J_{sm} \cos(\omega t - \alpha x) dx \tag{33}$$

where  $B_{y1}(t)$ —① air gap magnetic density,  $B_{y0}(t)$ —air gap magnetic density at  $x = 0$ ,  $\mu_0$  is the vacuum magnetic permeability,  $g_s$  is the equivalent air gap length after taking into account the slot effect and the static lateral side end effect. From Equation (33), the following equation can be obtained by the quadratic differential of  $x$ :

$$\frac{d^2 B_{y1}(t)}{dx^2} = -\frac{\mu_0 \alpha J_{sm}}{2g_s} \sin(\omega t - \alpha x) \tag{34}$$

Similarly, the magnetic field equations of the air gap in ② and ③ can be obtained:

$$\frac{d^2 B_{y2}(t)}{dx^2} = 0, \quad \frac{d^2 B_{y3}(t)}{dx^2} = 0 \tag{35}$$

where  $B_{y2}(t)$  and  $B_{y3}(t)$  are the magnetic density of the air gap in ② and ③, respectively. The boundary conditions satisfied by region ① ② ③ are:

$$\begin{cases} \frac{\partial B_{y2}(t)}{\partial x} \Big|_{x=-l} = \frac{\partial B_{y3}(t)}{\partial x} \Big|_{x=2l} = 0 \\ B_{y1}(t) - B_{y2}(t) \Big|_{x=0} = 0 \\ B_{y1}(t) - B_{y3}(t) \Big|_{x=l} = 0 \\ \int_{-l}^0 B_{y1}(t) dx + \int_{-l}^l B_{y2}(t) dx + \int_l^{2l} B_{y3}(t) dx = 0 \end{cases} \tag{36}$$

Applying Ampere’s law of loops at  $x = 0, l$

$$\begin{cases} -\frac{dB_{y1}(t)}{dx} + \frac{dB_{y2}(t)}{dx} = \frac{\mu_0 J_{sm}}{2g_s} \cos(\omega t - \alpha x) \\ -\frac{dB_{y1}(t)}{dx} + \frac{dB_{y3}(t)}{dx} = \frac{\mu_0 J_{sm}}{2g_s} \cos(\omega t - \alpha x) \end{cases} \tag{37}$$

From the above differential equations and the corresponding boundary conditions, we can obtain the air-gap magnetic field in each region in WS-PMLSM without considering the half-full slot and odd poles.

$$\begin{cases} B_{y1}(t) = B_m \cos(\omega t - \alpha x) - (-1)^{(p)} k_s B_m ch(\beta x) \cos \omega t + (-1)^{(p)} k_h B_m sh(\beta x) \cos \omega t \\ B_{y2}(t) = B_{y3}(t) = -(-1)^{(p)} k_s B_m \cos \omega t \\ \beta = \sqrt{\frac{2\mu_0}{g_s H_c \mu_{fe}}} \\ k_s = \frac{sh(\beta l)}{sh(\beta p \tau)} \end{cases} \tag{38}$$

When the iron core is not saturated  $\beta \approx 0, k_s = 2, k_h = 0$

$$B_{y1}(t) = B_m \cos(\omega t - \alpha x) - (-1)^{(p)} 2B_m \cos \omega t \tag{39}$$

From the above equation, it can be seen that due to the presence of unenergized segmented cores on both sides of the supply section, the magnetic field generated by each phase winding has a DC component in the energized segmented interval, resulting in a DC pulsating component in the synthesized magnetic field, forming a pulsating air-gap magnetic field. The effect of the length of the end core on the ratio of the pulsating magnetic field and the amplitude of the current traveling wave field formed by the static end effect can be expressed as:

$$k_{m1} = \frac{l \cos \omega t}{p\tau \cos(\omega t - \theta_0)} \tag{40}$$

From Equation (40), it can be seen that the longer the core length, the larger the amplitude of the pulsating magnetic field; increasing the number of pole pairs can suppress the effect of the end effect, and increasing the length of the single-section primary and decreasing the length ratio of the secondary and primary can weaken the effect of the end effect. For WS-PMSM, the phase imbalance characteristic is an important characterization of the longitudinal end effect of the primary module, which has a significant impact on the control characteristics of the motor.

#### 4. End Effects Caused by Secondary Finite Length

The secondary longitudinal end effect can also be called the secondary end effect. It is mainly manifested as the magnetic field of the secondary pole affecting the magnetic field distribution through the discontinuity of two adjacent stator sections, which in turn causes the thrust fluctuation of the motor.

##### Modeling of Secondary Longitudinal End Effects

To analyze the end magnetic field of the WS-PMLSM, the Schwarz–Christoffel transformation is used, and the specific variation process is shown in Figure 6a–c. In the derivation process, assuming that the scalar potential of the secondary is  $\omega = 1$  and the scalar potential of the primary armature core is  $\omega = -1$ , then there is a line of symmetry with a potential of  $\omega = 0$  at the center of the air gap, as shown in Figure 6a, and the problem can be reduced to a polygonal solution containing a right-angle coordinate system, such that by the Schwarz–Christoffel transformation and logarithmic transformation, the magnetic field in the  $z$ -plane can be turned into a semicircular region in the  $w$ -plane, and finally, into a region of parallel line segments in the  $t$ -plane to obtain a regular magnetic field pattern.

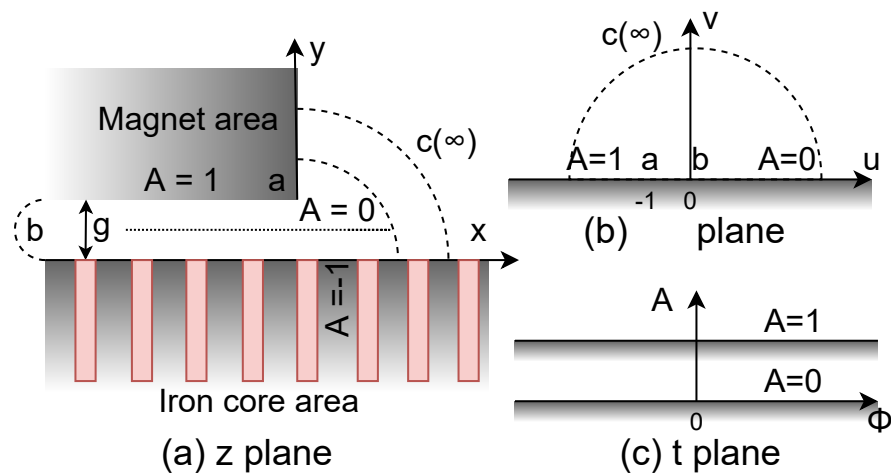


Figure 6. Coordinate plane of  $z - w - t$ .

The transformation between the  $z$ -plane,  $w$ -plane, and  $t$ -plane coordinate systems is performed according to Equation (41). The  $g$  in the equation represents the air gap.

$$\begin{cases} z \rightarrow w : z = \frac{g}{2\pi} \left[ 2(w+1)^{\frac{1}{2}} + \ln \frac{(w+1)^{\frac{1}{2}} - 1}{(w+1)^{\frac{1}{2}} + 1} \right] \\ w \rightarrow t : w = e^{\pi t} \quad \text{or} \quad t = \frac{1}{\pi} \ln w \\ z \rightarrow t : z = \frac{g}{\pi} \left[ \sqrt{2(e^{\pi t} + 1)} + \ln \frac{\sqrt{(e^{\pi t} + 1)} - 1}{\sqrt{(e^{\pi t} + 1)} + 1} \right] \end{cases} \tag{41}$$

In the  $t$ -plane, the magnetic field is regular and the magnetic induction at point  $b$  in the  $z$ -plane is considered to be maximum and uniform, and the magnetic potential set value  $A = 1$  yields  $B_{max} = 2\mu_0/g$  (in the  $z$ -plane, when passing through the point B, across the trip  $g/2$ ), then the magnetic density at any point within the end field is:

$$B = \mu_0 H = \mu_0 \left| \frac{dt}{dz} \right| = \mu_0 \left| \frac{dt}{dw} \frac{dw}{dz} \right| = B_{max} (w+1)^{-\frac{1}{2}} \tag{42}$$

The magnetic density distribution in this region varies with position in an exponential-like pattern, and the expression is obtained from the curve fitting.

$$B_{end} = \begin{cases} B_{max} e^{\frac{-x}{g_e}} & x \geq 0 \\ B_{max} e^{\frac{x + [(2p-1)\tau + L_m]}{g_e}} & x \leq -[(2p-1)\tau + L_m] \end{cases} \tag{43}$$

where  $g_e$  is the length of the electromagnetic air gap after the introduction of the cardinality factor. Then, the equivalent air gap length at the secondary end is:

$$g_{end} = \begin{cases} g_e e^{\frac{x}{g_e}} & x \geq 0 \\ g_e e^{\frac{-x - [(2p-1)\tau + L_m]}{g_e}} & x \leq -[(2p-1)\tau + L_m] \end{cases} \tag{44}$$

The change of the air-gap ratio permeability function with the position in this area can be obtained by curve fitting as follows [36]:

$$\frac{B_{end}}{B_{max}} = \begin{cases} 0.6635e^{-1.597x} + 0.2012e^{-0.2335x} & x > 0 \\ -0.1782e^{4.385x} + 1.009e^{0.0007946x} & -\tau < x \leq 0 \end{cases} \tag{45}$$

The influence of the end effect caused by the finite length of the permanent magnet on the air-gap magnetic field of WS-PMLSM is shown in Figure 7.

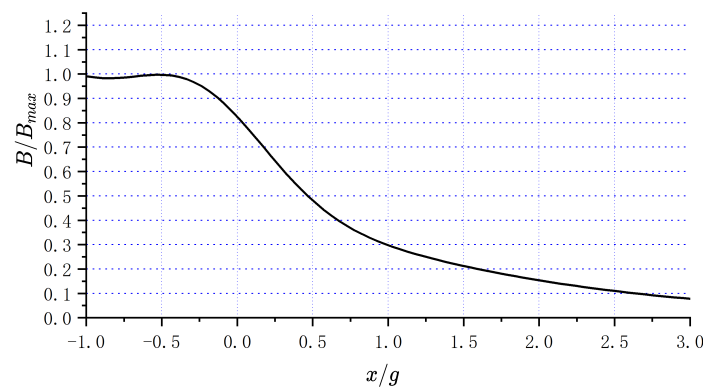


Figure 7. End effect of the air gap ratio permeability.

Figure 7 shows magnetic flux density normalized curve  $\frac{B}{B_{max}} = f\left(\frac{x}{g}\right)$  in the longitudinal end region. When  $x = -g$ , the magnetic inductance  $B_{max}$ , near the transverse edge of the armature core, and the magnetic inductance of the air gap gradually decays, and

when  $x = -0.25g$ ,  $B = 0.95B_{max}$ , the magnetic inductance decays to 95% of the maximum value. When  $x = 0$ , corresponding to the transverse edge of the armature core, i.e., point A in the  $z$ -plane, the magnetic inductance is  $B = 0.833B_{max}$ . That is, the original magnetic field is weakened, which corresponds to the generation of an additional magnetic field that weakens the main air gap field and causes a change in its distribution. When the WS-PMLSM is at no load, the additional magnetic field generated by the end effect is a constant. In terms of the magnetic circuit, the end effect changes the flux path of the end poles, the air-gap flux density under the surface of the end poles decreases, and the N-pole motor forms an  $(N + 1)$  magnetic circuit, as shown in Figure 8. Where  $B, B_1, B_2$  is  $B$  is the magnetic flux density test point,  $h_m$  is the permanent magnet height,  $g$  is the air gap length,  $h_s$  is the slot height,  $h_c$  is the height of the stator support.

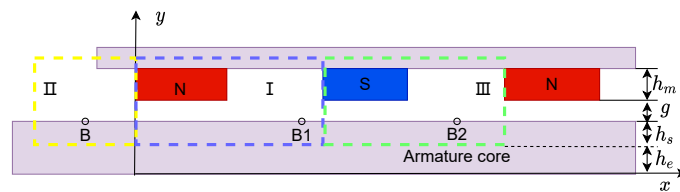


Figure 8. Analysis model of PM secondary end effects.

It can be seen that a total of three regions are generated: the end magnetic field region II ( $x < 0$ ) and the effective magnetic field region I ( $0 < x < \tau$ ), which forms an entire magnetic circuit system with area I and area III ( $\tau < x < 2\tau$ ).

## 5. Validation of the Analytical Methods by the FEM and Experiments

### 5.1. Finite Element Flux Simulation and Experimental Setup

In order to evaluate the merits of the proposed analytical model, the FEM method and experimental validation were used. The main parameters of the prototype are listed in Table 1. In the FEM analysis method, the material of the primary and secondary backing iron was steel-1010, and the JMAG software was used for modeling and simulation. A passive mover with a width of 150 mm and a stator with a length of 1000 mm were manufactured. The stator was composed of five sets of three-phase winding modules. The passive mover was supported by a linear bearing consisting of LM tracks. The passive mover at the origin of the permanent magnet was measured by a non-contact linear encoder.

Table 1. Structure parameters of PMSLM.

Parameters	Symbol	Value (Unit)
Length of the stator	$L_{stator}$	200 mm
Length of the mover	$L_{mover}$	200 mm
Air-gap length	$\delta$	1.5 mm
Height of slot opening	$H_s$	15 mm
Height of PM	$H_m$	4.0 mm
Height of the back core of PM	$H_{zc}$	4.0 mm
Height of the stator core	$H_{st}$	25 mm
Stator tooth width	$b_s$	4 mm
Slot pitch	$t_s$	8 mm
Pole pitch	$\tau$	50 mm
Relative permeability of PM	$\mu_r$	1.04
PM remanence	$B_r$	1.12 T
Number of armature teeth	$Z_p$	25
Number of pole pairs	$p$	1

Figure 9 shows the experimental prototype of the proposed system.

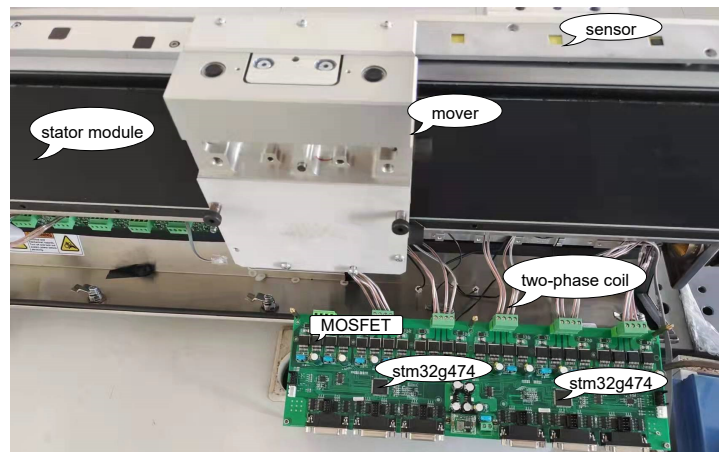


Figure 9. Experimental prototype of the proposed system.

Figure 10 shows the magnetic flux simulation. We chose full coverage and found that the two end effects and the tooth slot effect are very obvious. For further verification and comparison, the analytical solution and the finite element diagram are compared below.

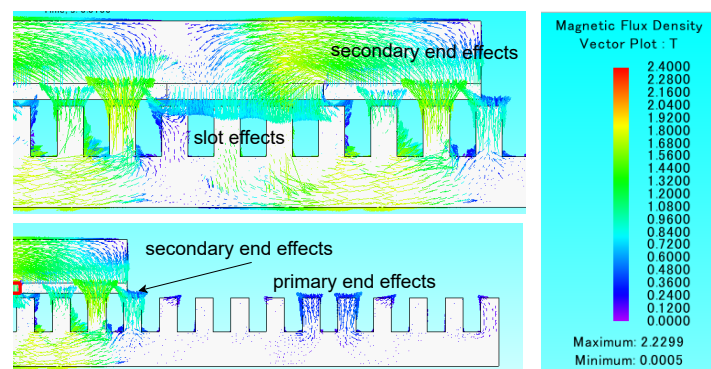


Figure 10. Flux simulation of WS-PMLSM using JMAG.

### 5.2. Slot Flux Density Distribution in Each Subdomain

The initial positions are chosen at three different locations, namely, the surface of the permanent magnet, the surface at the junction of the air gap and the tooth slot, and the center of the air gap. Their normal and tangential flux densities, as determined by the analytical results and the FEM simulations, are compared in Figures 11–13.

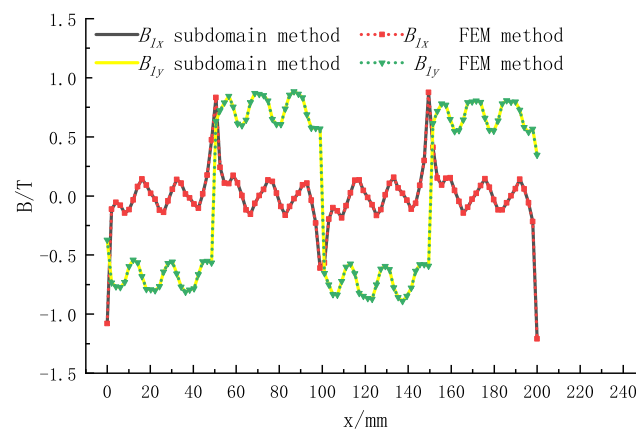
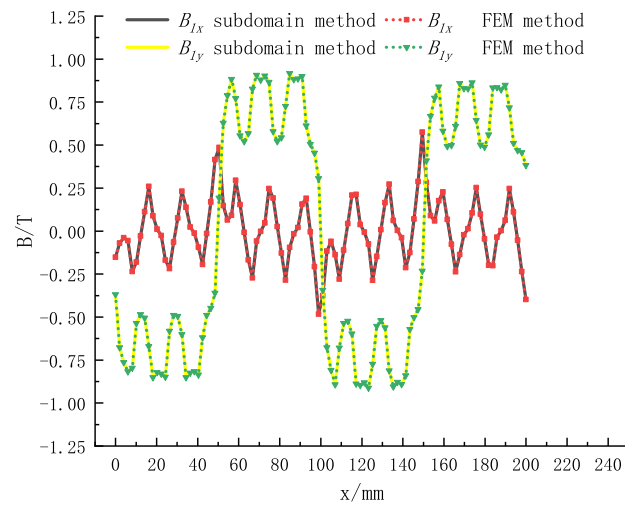
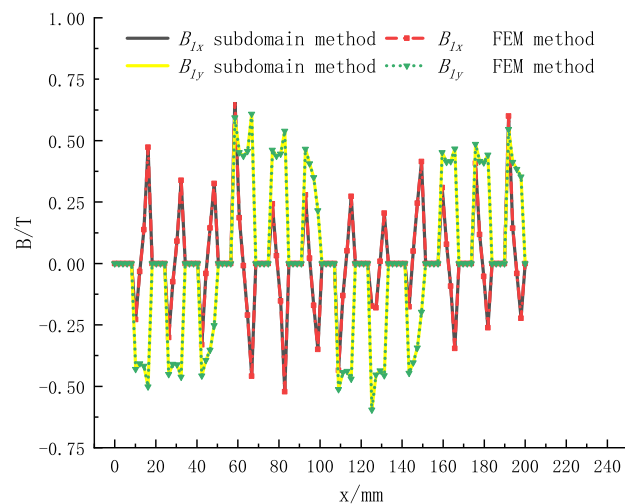


Figure 11. Permanent magnet surface flux density distribution.



**Figure 12.** Air gap center flux density distribution.



**Figure 13.** Slot surface flux density distribution.

It can be seen that the flux density of each subdomain obtained by the accurate subdomain analysis model basically overlaps with the finite element results, which proves the accuracy of the analysis method. From the above figure, it can be seen that the winding slotting causes the change of air gap permeability and the change of air-gap flux density integrates the effect of all slotting effects, and the closer to the slotting surface, the more obvious the slotting effect is.

### 5.3. End Effects Caused by PM

From Figure 14, it can be seen that the secondary end effect reduces the magnetic density of the air-gap field of the end magnets, resulting in an uneven distribution of the air-gap field under the surface of the pole plate. Due to the structural symmetry of the “outgoing” and “incoming” ends of the motor, the magnitude of the magnetic induction losses at the two ends is equal. At the same time, the secondary end effect of the air-gap magnetic field of the WS-PMLSM causes the flux path at the ends to change, while the magnetic induction strength of the air-gap under the pole surface at the ends decreases.

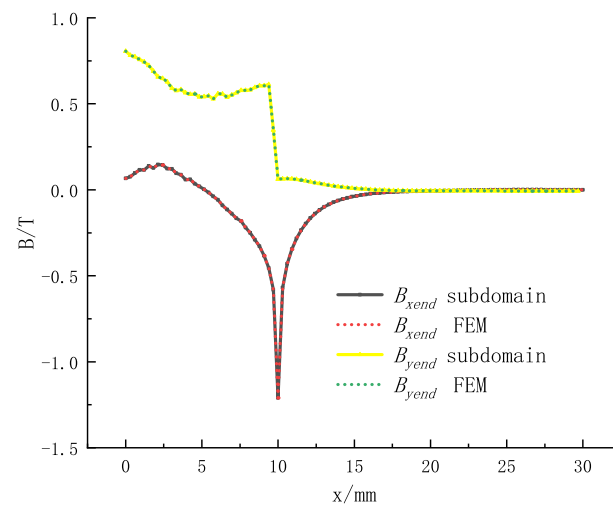


**Figure 14.** PM end density distribution.

#### 5.4. End Effects Caused by Winding Segmentation

As shown in Figure 15 below, when three symmetrical voltages are applied to the motor, the impedance of each phase of the motor is asymmetrical due to the effect of winding segmentation, which will lead to the asymmetrical three-phase current of the motor. The air-gap magnetic field of the motor is an asymmetrical magnetic field, and the positive sequence current component of the motor will generate positive direction electromagnetic thrust. The negative sequence current component of the motor will generate a reverse direction electromagnetic thrust. At the same time, it will produce the asymmetry of the motor inductance matrix and impedance matrix, which will cause the pulsation of the air gap magnetic field and thus the thrust fluctuation.

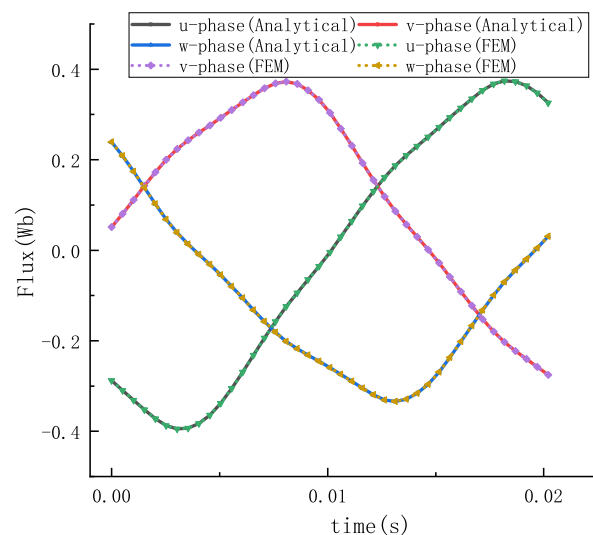


**Figure 15.** Flux with symmetrical voltage excited.

#### 5.5. Detent Force Calculation

On basis of the aforementioned analytical model, the  $x$ - and  $y$ -direction components of flux density can be accurately obtained. Using the Maxwell stress theory, the cogging force along the  $x$ -direction and the normal magnetic force along the  $y$ -direction caused by the effect of the slot and PM mover can be expressed as [37]

$$F_x = \frac{L_z}{\mu_0} \int_{x_1}^{x_2} B_{2x} B_{2y} dx$$

$$F_y = \frac{L_z}{2\mu_0} \int_{x_1}^{x_2} (B_{2y}^2 - B_{2x}^2) dx$$
(46)

where  $L_z$  is the longitudinal length of the linear motor along the  $z$ -direction, and  $B_x$  and  $B_y$  are the  $x$ - and  $y$ -direction components of flux density in region 2, respectively. The lower and upper limits of integration are  $x_1 = -\frac{L}{2}$  and  $x_2 = \frac{L}{2}$ , respectively. For the proposed analytical method, the distance between  $x_1$  and  $x_2$  includes the adjacent unit windings not energized at both sides of the mover, as shown in Figure 8.

Finally, the three effects were verified in practice on the experimental platform. We used a thrust test to verify the fluctuations caused by three conditions. The characteristics of the cogging force in the  $x$ - direction at different positions are shown in Figure 16. In the starting section, the deviation of the force is mainly caused by the end effect, then the amplitude decays as a function in the second transition section, and finally, it is completely generated by the slot in the third section. Fluctuations caused by the cogging effect are always present, which is in accordance with the experimental data.

The above results show that the cogging effect is caused by the structure and can be solved from the motor body design and control method, while the fluctuations generated by the end effect with high harmonics can be handled by the Taylor expansion method, which is not described here.

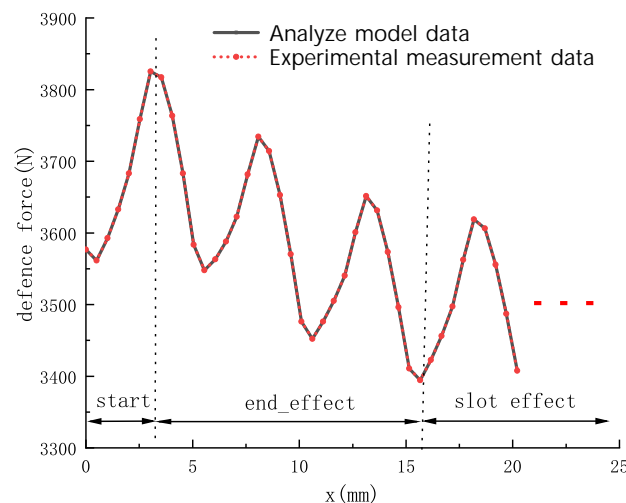


Figure 16. Detent force characteristics.

## 6. Conclusions

In this paper, the characteristic law of detent force in motor design and operation is revealed by the method of analytics with WS-PMLSM as the research object. The magnetic field analysis operation is carried out for two types of end effects and slot effects in the motor, which provides a theoretical basis for studying the fluctuation characteristics of electromagnetic force in this type of motor. The following research work is mainly accomplished in this paper.

(1) An accurate subdomain analysis model is proposed instead of the hierarchical model for solving the magnetic field distribution and thrust fluctuations of the slotted teeth of the WS-PMLSM motor. Using this analysis model, the magnetic field of the magnet, including the magnetized PM, and the effect of different slot widths on the thrust of the motor can be solved.

(2) For the end effect caused by the finite length of WS-PMLSM, the secondary is investigated, the longitudinal end effect formed by the permanent magnet secondary is equated with the edge effect at the end, and the Schwarz–Christoffel transform is used to solve such problem. This method is conventional but effective.

(3) In WS-PMLSM, the end effect caused by winding discontinuity is less studied. In this paper, Maxwell's equations are used to study it, and some conclusions are obtained; namely, under the action of three symmetrical voltages, the motor generates three-phase asymmetric currents, and negative sequence currents generate reverse electromagnetic thrust. The impedance matrix of the motor is not a cyclic symmetric array at this time, so the sequence impedance cannot be transformed into a diagonal array.

In the next step, the authors will compare the finite element analysis with experimental results for the conclusions obtained in this paper. Thanks to the expression of the WS-PMLSM cogging torque waveform, the rotor eddy current loss due to the cogging effect is completed in the next study. Since the local values of flux density or vector potential are not easy to measure, this experiment is not sufficient, but it is possible to compare the integral magnitude, such as counter-electromotive force or torque, which will be completed in the next study.

**Author Contributions:** Conceptualization, T.Z.; methodology, T.Z.; validation, T.Z. and X.M.; formal analysis, T.Z.; investigation, X.M.; writing—original draft preparation, T.Z.; writing—review and editing, X.M.; supervision, X.M.; funding acquisition, X.M. All authors have read and agreed to the published version of the manuscript.

**Funding:** This work was supported in part by the National Natural Science Foundation of China under the grant 51735010.

**Institutional Review Board Statement:** Not applicable.

**Informed Consent Statement:** Not applicable.

**Data Availability Statement:** The dataset can be accessed upon request to the corresponding author.

**Conflicts of Interest:** The authors declare no conflict of interest.

## Appendix A

From the boundary condition in Equation (22), the following equations can be given

$$\begin{cases} A_1(n) + B_1(n) = 0 \\ C_1(n) + D_1(n) = 0 \end{cases} \quad (\text{A1})$$

According to the boundary conditions in Equation (23), the following equations can be obtained:

$$\begin{cases} A_1(n)e^{k_n h_m} + B_1(n)e^{-k_n h_m} = A_2(n)e^{k_n h_m} + B_2(n)e^{-k_n h_m} \\ C_1(n)e^{k_n h_m} + D_1(n)e^{-k_n h_m} = C_2(n)e^{k_n h_m} + D_2(n)e^{-k_n h_m} \end{cases} \quad (\text{A2})$$

From the boundary condition Equations (1) and (23), the following equations can be obtained:

$$\begin{cases} \mu_r k_n [A_1(n)e^{k_n h_m} - B_1(n)e^{-k_n h_m}] - M_{xcn} = \\ k_n [A_2(n)e^{k_n h_m} - B_2(n)e^{-k_n h_m}] \\ \mu_r k_n [C_1(n)e^{k_n h_m} - D_1(n)e^{-k_n h_m}] - M_{xsn} = \\ k_n [C_2(n)e^{k_n h_m} - D_2(n)e^{-k_n h_m}] \end{cases} \quad (\text{A3})$$

From the boundary condition Equation (24), the magnetic potential at the slot surface and air gap boundary is continuous

$$\phi_2(x, y)|_{y=h_m+\delta} = \phi_s(x, y) \quad (\text{A4})$$

$$\begin{aligned} \phi_s(x, y) = \phi_{3i}(x, y)|_{y=h_m+\delta} = \\ \begin{cases} \phi_{3i}(x, y)|_{y=h_m+\delta} & x \in [x_i, x_i + b_s] \\ 0 & \text{other} \end{cases} \end{aligned} \quad (\text{A5})$$

According to Equation (18)

$$\begin{aligned} \phi_2(x, y)|_{y=h_m+\delta} = & \\ \sum_{n=1,2,\dots}^{\infty} \left[ A_2(n)e^{k_n(h_m+\delta)} + B_2(n)e^{-k_n(h_m+\delta)} \right] \cos(k_n x) + & \\ \sum_{n=1,2,\dots}^{\infty} \left[ C_2(n)e^{k_n(h_m+\delta)} + D_2(n)e^{-k_n(h_m+\delta)} \right] \sin(k_n x) & \end{aligned} \tag{A6}$$

The magnetic level on the surface of the slot is

$$\begin{aligned} \phi_s(x, y) = \phi_{3i}(x, y)|_{y=h_m+\delta} & \\ = \sum_{m=1,2,\dots}^{\infty} C_{3i}(m)\chi_m \sin[F_m(x - x_i)] & \\ = \sum_{m=1,2,\dots}^{\infty} C_{ei}(m) \sin[F_m(x - x_i)] \quad x \in [x_i, x_i + b_s] & \end{aligned} \tag{A7}$$

where

$$C_{ei}(m) = C_{3i}(m)\chi_m \quad \chi_m = e^{F_m(h_m+\delta)}(1 - e^{2F_m h_s}) \tag{A8}$$

The magnetic position of the tooth surface is

$$\phi_s(x, y) = 0 \quad x \notin [x_i, x_i + b_s] \tag{A9}$$

The Fourier series expansion of  $\phi_s(x, y)$

$$\phi_s(x, y) = \sum_{n=1}^{\infty} [A_s(n) \cos(k_n x) + B_s(n) \sin(k_n x)] \tag{A10}$$

Although the period of the slot is not the same as the harmonic period of the PM, at boundary condition Equation (23), the harmonics of  $\phi_2(x, y)$  originate from the PM, so the period of the Fourier expansion is the period of the PM.

$$\begin{aligned} A_s(n) = & \\ \frac{1}{\tau} \int_{x_i}^{x_i+b_s} \sum_{m=1,2,\dots}^{\infty} C_{3i}(m)\chi_m \sin[F_m(x - x_i)] \cos(k_n x) dx & \\ = \sum_{i=1}^{z_p} \sum_{m=1,2,\dots}^{\infty} C_{3i}(m)\chi_m \eta_{si}(m, n) & \end{aligned} \tag{A11}$$

$$\begin{aligned} B_s(n) = & \\ \frac{1}{\tau} \int_{x_i}^{x_i+b_s} \sum_{m=1,2,\dots}^{\infty} C_{3i}(m)\chi_m \sin[F_m(x - x_i)] \sin(k_n x) dx & \\ = \sum_{i=1}^{z_p} \sum_{m=1,2,\dots}^{\infty} C_{3i}(m)\chi_m \zeta_{si}(m, n) & \end{aligned} \tag{A12}$$

$$\eta_{si}(m, n) = \eta_s(m, n) \cos(k_n x_i) - \zeta_s(m, n) \sin(k_n x_i) \tag{A13}$$

$$\zeta_{si}(m, n) = \eta_s(m, n) \sin(k_n x_i) + \zeta_s(m, n) \cos(k_n x_i) \tag{A14}$$

in the formula

$$\eta_s(m, n) = \begin{cases} \frac{mb_s\tau[1-\cos(m\pi)\cos(k_nb_s)]}{\pi(m^2\tau^2-n^2b_s^2)} & m\tau \neq nb_s \\ -\frac{b_s}{2\tau} \sin\left(m\frac{\pi}{b_s}x_i\right) & m\tau = nb_s \end{cases} \tag{A15}$$

$$\zeta_s(m, n) = \begin{cases} \frac{-mb_s\tau \cos(m\pi) \sin(k_nb_s)}{\pi(m^2\tau^2-n^2b_s^2)} & m\tau \neq nb_s \\ \frac{b_s}{2\tau} \cos\left(m\frac{\pi}{b_s}x_i\right) & m\tau = nb_s \end{cases} \tag{A16}$$

According to the boundary conditions Equation (24), the following equation set can be obtained:

$$\begin{cases} A_2(n)e^{k_n(h_m+\delta)} + B_2(n)e^{-k_n(h_m+\delta)} = A_s(n) = \\ \sum_{i=1}^{z_p} \sum_{m=1,2,\dots}^{\infty} C_{3i}(m)\chi_m \eta_{si}(m, n) \\ C_2(n)e^{k_n(h_m+\delta)} + D_2(n)e^{-k_n(h_m+\delta)} = B_s(n) = \\ \sum_{i=1}^{z_p} \sum_{m=1,2,\dots}^{\infty} C_{3i}(m)\chi_m \zeta_{si}(m, n) \end{cases} \tag{A17}$$

From the boundary condition Equation (24), the normal magnetic flux density at the surface boundary of the air gap subdomain and the tooth slot subdomain is continuous.

$$\begin{aligned}
 B_{2y}|_{y=h_m+\delta} &= -\mu_0 \frac{\partial \phi_2}{\partial y} \Big|_{y=h_m+\delta} = \\
 &-\mu_0 \sum_{n=1,2}^{\infty} k_n \left[ A_2(n) e^{k_n(h_m+\delta)} - B_2(n) e^{-k_n(h_m+\delta)} \right] \\
 \cos(k_n x) &- \mu_0 \sum_{n=1,2}^{\infty} k_n \left[ C_2(n) e^{k_n(h_m+\delta)} - D_2(n) e^{-k_n(h_m+\delta)} \right] \\
 \sin(k_n x) &
 \end{aligned}
 \tag{A18}$$

$$\begin{aligned}
 B_{3iy}|_{y=h_m+\delta} &= -\mu_0 \frac{\partial \phi_3}{\partial y} \Big|_{y=h_m+\delta} \\
 &= -\mu_0 \sum_{m=1,2\dots}^{\infty} C_{3i}(m) \delta_m \sin[F_m(x - x_i)]
 \end{aligned}
 \tag{A19}$$

in the formula

$$\delta_m = F_m e^{F_m(h_m+\delta)} (1 + e^{2F_m h_s})
 \tag{A20}$$

Since  $B_{2y}$  is in the form of a general solution, a Fourier series expansion is made at the  $i$ -th slotted region ( $x_i \leq x \leq x_i + b_s$ )

$$\begin{aligned}
 B_{2y}|_{y=h_m+\delta} &= -\mu_0 \sum_{m=1,2,\dots}^{\infty} C_{si}(m) \sin[F_m(x - x_i)] \\
 x &\in [x_i, x_i + b_s]
 \end{aligned}
 \tag{A21}$$

where

$$\begin{aligned}
 C_{si}(m) &= \\
 &\frac{2}{b_s} \int_{x_i}^{x_i+b_s} \sum_{n=1,2}^{\infty} k_n \left[ A_2(n) e^{k_n(h_m+\delta)} - B_2(n) e^{-k_n(h_m+\delta)} \right] \\
 &\cos(k_n x) \sin[F_m(x - x_i)] dx + \\
 &\frac{2}{b_s} \int_{x_i}^{x_i+b_s} \sum_{n=1,2}^{\infty} k_n \left[ C_2(n) e^{k_n(h_m+\delta)} - D_2(n) e^{-k_n(h_m+\delta)} \right] \\
 &\sin(k_n x) \sin[F_m(x - x_i)] dx
 \end{aligned}
 \tag{A22}$$

Simplifying  $C_{si}(m)$  yields

$$\begin{aligned}
 C_{si}(m) &= \\
 &\sum_{n=1,2}^{\infty} k_n \left[ A_2(n) e^{k_n(h_m+\delta)} - B_2(n) e^{-k_n(h_m+\delta)} \right] \sigma_{si}(m, n) + \\
 &\sum_{n=1,2}^{\infty} k_n \left[ C_2(n) e^{k_n(h_m+\delta)} - D_2(n) e^{-k_n(h_m+\delta)} \right] \tau_{si}(m, n)
 \end{aligned}
 \tag{A23}$$

$$\sigma_{si}(m, n) = \frac{2\tau}{b_s} \eta_{si}(m, n)
 \tag{A24}$$

$$\tau_{si}(m, n) = \frac{2\tau}{b_s} \xi_{si}(m, n)
 \tag{A25}$$

According to the boundary condition Equation (24),

$$\begin{aligned}
 \delta_m C_{3i}(m) &= C_{si}(m) = \\
 &\sum_{n=1,2}^{\infty} k_n \left[ A_2(n) e^{k_n(h_m+\delta)} - B_2(n) e^{-k_n(h_m+\delta)} \right] \sigma_{si}(m, n) + \\
 &\sum_{n=1,2}^{\infty} k_n \left[ C_2(n) e^{k_n(h_m+\delta)} - D_2(n) e^{-k_n(h_m+\delta)} \right] \tau_{si}(m, n)
 \end{aligned}
 \tag{A26}$$

Summarizing the above equations, they can be concentrated as Equation (A27).

Afterward, these equations can be converted to matrix form. There are three parameters in the matrix  $m, n, i$ , where  $m$  is the harmonic coefficient of the stator slot. The larger  $m$  is, the more clearly the interaction between the slots will be revealed.  $n$  is the harmonic coefficient of the PM, and  $i$  is the number of slots, so the dimension of the matrix is  $m \times n$ . In order to solve the convenient, the following formula is  $n = 1, m = 25$ , as in Equation (A28).

Therefore, when  $n$  is taken in the range that it can be, it is possible to solve for the possible coefficients.

$$\left\{ \begin{array}{l}
 A_1(n) + B_1(n) = 0 \\
 C_1(n) + D_1(n) = 0 \\
 A_1(n)e^{K_n h_m} + B_1(n)e^{-K_n h_m} - A_2(n)e^{K_n h_m} - B_2(n)e^{-K_n h_m} = 0 \\
 C_1(n)e^{K_n h_m} + D_1(n)e^{-K_n h_m} - C_2(n)e^{K_n h_m} - D_2(n)e^{-K_n h_m} = 0 \\
 \mu_r A_1(n)e^{K_n h_m} - \mu_r B_1(n)e^{-K_n h_m} - A_2(n)e^{K_n h_m} + B_2(n)e^{-K_n h_m} = \frac{1}{K_n} M_{xnc} \\
 \mu_r C_1(n)e^{K_n h_m} - \mu_r D_1(n)e^{-K_n h_m} - C_2(n)e^{K_n h_m} + D_2(n)e^{-K_n h_m} = \frac{1}{K_n} M_{xns} \\
 A_2(n)e^{K_n(h_m+\delta)} + B_2(n)e^{-K_n(h_m+\delta)} - \sum_i \sum_m D_{3i}(m)e^{-F_m(h_m+\delta)} \eta_{si}(m, n) = 0 \\
 C_2(n)e^{K_n(h_m+\delta)} + D_2(n)e^{-K_n(h_m+\delta)} - \sum_i \sum_m D_{3i}(m)e^{-F_m(h_m+\delta)} \delta_{si}(m, n) = 0 \\
 \frac{2\tau}{b_s} \sum_i \sum_n K_n \left\{ \begin{array}{l}
 [A_2(n)e^{K_n y_3} - B_2(n)e^{-K_n(h_m+\delta)}] \eta_{si}(m, n) \\
 + [C_2(n)e^{K_n(h_m+\delta)} - D_2(n)e^{-K_n(h_m+\delta)}] \delta_{si}(m, n)
 \end{array} \right\} + F_m D_3(m)e^{-F_m(h_m+\delta)} = 0
 \end{array} \right. \tag{A27}$$

$$\begin{bmatrix}
 1 & 1 & 0 & 0 & 0 & 0 & 0 & 0 & 0 \\
 0 & 0 & 1 & 1 & 0 & 0 & 0 & 0 & 0 \\
 E_{3nn} & E_{4nn} & 0 & 0 & E_{5nn} & E_{6nn} & 0 & 0 & 0 \\
 0 & 0 & E_{3nn} & E_{4nn} & 0 & 0 & E_{5nn} & E_{6nn} & 0 \\
 E_{7nn} & E_{8nn} & 0 & 0 & E_{9nn} & E_{10nn} & 0 & 0 & 0 \\
 0 & 0 & E_{7nn} & E_{8nn} & 0 & 0 & E_{9nn} & E_{10nn} & 0 \\
 0 & 0 & 0 & 0 & E_{11nn} & E_{12nn} & 0 & 0 & E_{17Snn} \\
 0 & 0 & 0 & 0 & 0 & 0 & E_{11nn} & E_{12nn} & E_{18Snn} \\
 0 & 0 & 0 & 0 & E_{13Snn} & E_{14Snn} & E_{15Snn} & E_{16Snn} & W_{mm}
 \end{bmatrix}
 \begin{bmatrix}
 A_1 \\
 B_1 \\
 C_1 \\
 D_1 \\
 A_2 \\
 B_2 \\
 C_2 \\
 D_2 \\
 D_3
 \end{bmatrix}
 =
 \begin{bmatrix}
 0 \\
 0 \\
 0 \\
 0 \\
 B_{b5} \\
 B_{b6} \\
 0 \\
 0 \\
 0 \\
 0
 \end{bmatrix} \tag{A28}$$

$$\begin{aligned}
 E_{3nn}(n, n) &= e^{K_n h_m}, & E_{4nn}(n, n) &= e^{-K_n h_m} \\
 E_{5nn}(n, n) &= -e^{K_n h_m}, & E_{6nn}(n, n) &= -e^{-K_n h_m} \\
 E_{7nn}(n, n) &= \mu_r e^{K_n h_m}, & E_{8nn}(n, n) &= -\mu_r e^{-K_n h_m} \\
 E_{9nn}(n, n) &= -e^{K_n h_m}, & E_{10nn}(n, n) &= e^{-K_n h_m} \\
 E_{11nn}(n, n) &= e^{K_n(h_m+\delta)}, & E_{12nn}(n, n) &= e^{-K_n(h_m+\delta)}
 \end{aligned} \tag{A29}$$

$$\begin{aligned}
 E_{13Snn} &= \sum_i \sum_n \frac{2T_p P}{b} K_n e^{K_n(h_m+\delta)} \eta_{si}(m, n) \\
 E_{14Snn} &= \sum_i \sum_n -\frac{2T_p P}{b} K_n e^{-K_n(h_m+\delta)} \eta_{si}(m, n)
 \end{aligned} \tag{A30}$$

$$\begin{aligned}
 E_{15Snn} &= \sum_i \sum_n \frac{2T_p P}{b} K_n e^{K_n(h_m+\delta)} \delta_{si}(m, n) \\
 E_{16Snn} &= \sum_i \sum_n -\frac{2T_p P}{b} K_n e^{-K_n(h_m+\delta)} \delta_{si}(m, n) \\
 E_{17Snn} &= \sum_i \sum_m -e^{-F_m(h_m+\delta)} \eta_{si}(m, n) \\
 E_{18Snn} &= \sum_i \sum_m -e^{-F_m(h_m+\delta)} \delta_{si}(m, n)
 \end{aligned} \tag{A31}$$

$$\begin{aligned}
 W_{mm}(m_i, m_i) &= F_m e^{-F_m(h_m+\delta)} \\
 B_{b5} &= \frac{1}{K_n} M_{xnc}, & B_{b6} &= \frac{1}{K_n} M_{xns} \\
 D_3 &= \{D_{3i}\} \quad (i = 1, 2, \dots, z_n)
 \end{aligned} \tag{A32}$$

where  $z_n$  is the number of stator slots. The equations can be solved by matrix operations, which is a systematic and complex project due to its implementation by computer programming and will not be expanded on here.

**References**

- Mihalachi, M.; Leidhold, R.; Mutschler, P. Motion Control for Long Primary Linear Drives Used in Material Handling. In Proceedings of the 14th International Power Electronics and Motion Control Conference EPE-PEMC 2010, Ohrid, Macedonia, 6–8 September 2010; pp. T5-94–T5-101.

2. Ranky, P.G. MagneMotion's linear synchronous motor (LSM) driven assembly automation and material handling system designs. *Assem. Autom.* **2007**, *27*, 97–102. [[CrossRef](#)]
3. Zhang, T.; Mei, X.; Du, X. Absolute Position Acquisition for Linear Synchronous Motor With Passive Mover. *IEEE Access* **2021**, *9*, 100757–100768. [[CrossRef](#)]
4. Wang, M.; Li, L.; Pan, D. Detent Force Compensation for PMLSM Systems Based on Structural Design and Control Method Combination. *IEEE Trans. Ind. Electron.* **2015**, *62*, 6845–6854. [[CrossRef](#)]
5. Huang, Q.; Huang, X.; Yu, W.; Ren, C. Modeling and Optimization of Detent Force for Flexible Permanent Magnet Synchronous Linear Motor Considering Spacing Between Primaries. In Proceedings of the 2021 13th International Symposium on Linear Drives for Industry Applications (LDIA), Wuhan, China, 1–3 July 2021.
6. Shi, H.; Niguchi, N.; Hirata, K. Design and analysis of surface permanent magnet vernier linear motor based on air gap magnetic flux density distribution. In Proceedings of the 2019 12th International Symposium on Linear Drives for Industry Applications (LDIA), Neuchatel, Switzerland, 1–3 July 2019; IEEE: Piscataway, NJ, USA, 2019; pp. 1–5.
7. Huang, X.; Tianpeng, J.; Li, L.; Zhou, B.; Zhang, Z.; Gerada, D.; Gerada, C. Detent Force, Thrust, and Normal Force of the Short-Primary Double-Sided Permanent Magnet Linear Synchronous Motor With Slot-Shift Structure. *IEEE Trans. Energy Convers.* **2019**, *34*, 1411–1421. [[CrossRef](#)]
8. Zahid, A.; Khan, F.; Ahmad, N.; Sami, I.; Alkhamash, H.I. Design and Analysis of Dual Mover Multi-Tooth Permanent Magnet Flux Switching Machine for Ropeless Elevator Applications. *Actuators* **2021**, *10*, 81. [[CrossRef](#)]
9. Huang, X.; Liang, J.; Zhenyu, Q.; Li, J. An Iterative Estimation Algorithm of Prepositioning Focusing on the Detent Force in the Permanent Magnet Linear Synchronous Motor System. *IEEE Trans. Ind. Electron.* **2020**, *67*, 8252–8261. [[CrossRef](#)]
10. Benavides Oswald, R. Investigation of Control Methods for Segmented Long Stator Linear Drives. Ph.D. Thesis, Technische Universität, Berlin, Germany, 2008.
11. Cui, L.; Zhang, H.; Jiang, D. Research on High Efficiency V/f Control of Segment Winding Permanent Magnet Linear Synchronous Motor. *IEEE Access* **2019**, *7*, 138904–138914. [[CrossRef](#)]
12. Lines, C.R. Modelling and Control of Segmented Long-Stator Permanent-Magnet Linear Synchronous Motors. Ph.D. Thesis, University of the Witwatersrand, Faculty of Engineering and the Built, Johannesburg, South Africa, 2013.
13. Creppe, R.C.; Ulson, J.C.; Rodrigues, J.F. Influence of Design Parameters on Linear Induction Motor End Effect. *IEEE Trans. Energy Convers.* **2008**, *23*, 358–362. [[CrossRef](#)]
14. Lu, J.; Ma, W. Research on End Effect of Linear Induction Machine for High-Speed Industrial Transportation. *IEEE Trans. Plasma Sci.* **2011**, *39*, 116–120. [[CrossRef](#)]
15. Boff, B.H.B.; Eckert, P.R.; Amara, Y. A Comprehensive Review on the End Effects of Linear Permanent Magnet Machines. In Proceedings of the 2021 13th International Symposium on Linear Drives for Industry Applications (LDIA), Wuhan, China, 1–3 July 2021; IEEE: Piscataway, NJ, USA, 2021; pp. 1–6.
16. Benavides, R.; Mutschler, P. Detent force compensation in segmented long stator permanent magnet linear drives using Finite Element Models. In Proceedings of the European Conference on Power Electronics & Applications, Aalborg, Denmark, 2–5 September 2007.
17. Cui, F.; Sun, Z.; Xu, W.; Qian, H.; Cao, C. Optimization Analysis of Long Primary Permanent Magnet Linear Synchronous Motor. *IEEE Trans. Appl. Supercond.* **2021**, *31*, 1–4. [[CrossRef](#)]
18. Heidary, M.; Naderi, P.; Shiri, A. Modeling and analysis of a multi-segmented linear permanent-magnet synchronous machine using a parametric magnetic equivalent circuit. *Electr. Eng.* **2022**, *104*, 705–715. [[CrossRef](#)]
19. Bianchi, N. Analytical field computation of a tubular permanent-magnet linear motor. *IEEE Trans. Magn.* **2000**, *36*, 3798–3801. [[CrossRef](#)]
20. Yudin, M.; Sevostyanov, N.; Tsareva, D. Simulation of Electromagnetic Fields in Layered Media Based on Semi-Analytical Integral Transformations. *Conf. Proc.* **2021**, *2021*, 1–6.
21. Huangfu, Y.; Wang, S.; Qiu, J.; Zhang, H.; Wang, G.; Zhu, J. Transient Performance Analysis of Induction Motor Using Field-Circuit Coupled Finite-Element Method. *IEEE Trans. Magn.* **2014**, *50*, 873–876. [[CrossRef](#)]
22. Maroufian, S.S. Winding Function Modeling of Synchronous Reluctance Machines. Ph.D. Thesis, Concordia University, Montreal, QC, Canada, 2018.
23. Lakshmi, N.S.; Allirani, S. *Modelling and Simulation of Permanent Magnet Synchronous Motor for Performance Enhancement Using ANSYS Maxwell*; Springer: Berlin/Heidelberg, Germany, 2021.
24. Liu, Z.; Li, J. Accurate Prediction of Magnetic Field and Magnetic Forces in Permanent Magnet Motors Using an Analytical Solution. *IEEE Trans. Energy Convers.* **2008**, *23*, 717–726. [[CrossRef](#)]
25. Hu, H.; Zhao, J.; Liu, X.; Guo, Y.; Zhu, J. No-Load Magnetic Field and Cogging Force Calculation in Linear Permanent-Magnet Synchronous Machines With Semiclosed Slots. *IEEE Trans. Ind. Electron.* **2017**, *64*, 5564–5575. [[CrossRef](#)]
26. Lu, Q.; Wu, B.; Yao, Y.; Shen, Y.; Jiang, Q. Analytical model of permanent magnet linear synchronous machines considering end effect and slotting effect. *IEEE Trans. Energy Convers.* **2019**, *35*, 139–148. [[CrossRef](#)]
27. Chen, F.; Zhang, C.; Chen, J.; Yang, G. Accurate Subdomain Model for Computing Magnetic Field of Short Moving-Magnet Linear Motor With Halbach Array. *IEEE Trans. Magn.* **2020**, *56*, 8200509. [[CrossRef](#)]
28. Markovic, M.; Jufer, M.; Perriard, Y. Reducing the cogging torque in brushless DC motors by using conformal mappings. *IEEE Trans. Magn.* **2004**, *40*, 451–455. [[CrossRef](#)]

29. O'Connell, T.C.; Krein, P.T. A Schwarz–Christoffel-Based Analytical Method for Electric Machine Field Analysis. *IEEE Trans. Energy Convers.* **2009**, *24*, 565–577. [[CrossRef](#)]
30. Liyi, L.; Hong, J.; Lu, Z.; Ying, L.; Song, Y.; Rizhong, L.; Xiaopeng, L. Fields and Inductances of the Sectioned Permanent-Magnet Synchronous Linear Machine Used in the EMALS. *IEEE Trans. Plasma Sci.* **2011**, *39*, 87–93. [[CrossRef](#)]
31. Tursini, M.; Villani, M.; Tullio, A.D.; Fabri, G.; Collazzo, F.P. Nonlinear Model Suitable for the Offline Cosimulation of Fault-Tolerant PM Motors Drives. *IEEE Trans. Ind. Appl.* **2017**, *53*, 3719–3729. [[CrossRef](#)]
32. Benavides, R.; Mutschler, P. Compensation of Disturbances in Segmented Long Stator Linear Drives using Finite Element Models. In Proceedings of the International Symposium on Industrial Electronics, Montreal, QC, Canada, 9–13 July 2006.
33. Mihalachi, M.; Leidhold, R.; Mutschler, P. Linear drive system for combined transportation and processing of materials. In Proceedings of the Conference of the Industrial Electronics Society, Porto, Portugal, 3–5 November 2009.
34. Gysen, B.L.J.; Meessen, K.J.; Paulides, J.J.H.; Lomonova, E.A. General Formulation of the Electromagnetic Field Distribution in Machines and Devices Using Fourier Analysis. *IEEE Trans. Magn.* **2010**, *46*, 39–52. [[CrossRef](#)]
35. Liu, Z.; Li, J. Analytical Solution of Air-Gap Field in Permanent-Magnet Motors Taking Into Account the Effect of Pole Transition Over Slots. *IEEE Trans. Magn.* **2007**, *43*, 3872–3883. [[CrossRef](#)]
36. Mao, Y.; Sun, Z.; Zhou, W.; Cui, F. Equivalent Circuit Model of Long Primary Permanent Magnet Linear Synchronous Motor Considering End Effect. In Proceedings of the 2021 13th International Symposium on Linear Drives for Industry Applications (LDIA), Wuhan, China, 1–3 July 2021.
37. Virtic, P.; Stumberger, B. Analytical Analysis of Magnetic Field and Force Calculation in a Slotless-Type Permanent Magnet Linear Synchronous Machine; Verification with Numerical Analysis. In Proceedings of the International Electric Machines and Drives Conference, Antalya, Turkey, 3–5 May 2007.